JOURNAL OF PROPULSION AND POWER
Vol. 18, No. 3, May–June 2002

Appearance of Restricted Shock Separation in Rocket Nozzles

G. Hagemann*
Astrium GmbH, D-81663 Munich, Germany
and
M. Frey† and W. Koschel‡
DLR, German Aerospace Center, D-74239 Hardthausen, Germany

Uncontrolled flow separation in nozzles of rocket engines is not desired because it can lead to dangerous lateral forces. Different origins for side loads were identified in the past. Meanwhile, it is proven that in thrust-optimized or parabolic nozzles, a major side load occurs as a result of the transition of separation pattern from free shock separation to restricted shock separation and vice versa. Reasons for the transition between the separation patterns are discussed, and the cap-shock pattern, which is identified to be the cause of this transition, is closely analyzed. It turns out that this pattern can be interpreted as an inverse Mach reflection of the internal shock at the nozzle axis. To prove the transition effect as main side-load driver, a subscale test campaign has been performed. Two different nozzle contours, a thrust-optimized and a truncated ideal nozzle with equal performance data, were tested. Highest side loads were measured in the thrust-optimized nozzle, when the separation pattern changes from free to restricted shock separation. Side loads measured in the truncated ideal nozzle were only about one-third as high as in the thrust-optimized nozzle.

Nomenclature

I_{sp}	=	specific impulse
l	=	length
p_a	=	ambient pressure
p_c	=	chamber pressure
p_w	=	wall pressure
r_t	=	throat radius
x	=	length
γ	=	ratio of specific heats
ε	=	area ratio
θ	=	flow deflection angle across oblique shock
ϕ	=	flow angle

Introduction

UNCONTROLLED flow separation in rocket nozzles occurs whenever the wall pressure p_w is much lower than the ambient pressure p_a. Many publications dating from the 1950s and 1960s report about free shock separation (FSS) in nozzles, where the separated flow continues as a freejet (see Fig. 1). However, subscale testing of the J-2S engine[1] showed that for a certain range of pressure ratios a different kind of separation pattern existed, where the flow reattached to the wall downstream of the separation point, thereby forming a closed recirculation bubble. This flow type, which is illustrated in Fig. 2, was called restricted shock separation (RSS). Because RSS was only observed in subscale experiments with cold air for a long time, it was erroneously assumed that a reattachment never occurred in full-scale rocket engines and that in full-scale nozzles only FSS occurred.[2]

Side loads have been observed both in subscale and full-scale rocket nozzles during transient operations like startup or shutdown and during stationary operation with separated flow inside the nozzle. The first important report dealing with side forces was published in the frame of the J-2S development.[1] The side loads, which act in a direction perpendicular to the main thrust direction, represent a severe design constraint for new rocket engine concepts. Side loads in rocket nozzles can have different origins, and hence different models have been developed for their prediction. Potential origins for aerodynamic side loads are 1) a globally asymmetric separation line, 2) pressure pulsations at the separation location and downstream, 3) an aeroelastic coupling, 4) a transition of separation pattern in thrust-optimized or parabolic nozzles, and 5) external flow instabilities (also called buffeting, not considered in this discussion).

A review of different models, which have been developed based on the origins just listed, is included in Refs. 3 and 4. Although most of the models were able to predict the side-load level for one certain nozzle contour type, none of them were able to give correct predictions for a greater variety of different nozzle types.[2,4] This indicates that the magnitude of side-loads strongly depends on the nozzle contour and that this contour type has to be included into new models.

It was reported for thrust-optimized subscale nozzles that changes in separation pattern, namely the FSS → RSS and RSS → FSS transitions, lead to significant lateral forces.[1] Because of the erroneous assumption that RSS could only occur in subscale nozzles, the possibility was ruled out that such a transition could be the origin of side loads in full-scale rocket engines.

It has recently been shown by the authors that a specific shock pattern adapting the overexpanded exhaust flow to the ambient pressure, which is called cap-shock pattern, can exist in the plume of overexpanded thrust-optimized or parabolic nozzles with internal shock under full-flowing conditions.[5] This pattern is well visible in both subscale and full-scale nozzle tests (e.g., see Ref. 3–8). Figure 3 proves its existence in the plume of the Vulcain engine. First schlieren images of the cap-shock structure were published in the literature, but without looking at further details of its existence (e.g., Ref. 9). For lower pressure ratios p_c/p_a, when the flow is strongly overexpanded and separates inside the nozzle this flow

Received 20 November 1999; revision received 18 June 2001; accepted for publication 18 July 2001.

*Project Manager and Research Engineer, Space Infrastructure Division, P.O. Box 801168; gerald.hagemann@astrium-space.com. Member AIAA.

†Research Engineer, Space Propulsion, Lampoldshausen Research Center; currently Research Engineer, Volvo Aero Corporation, Space Propulsion Division, 6660 NY, 46181 Trollhättan, Sweden; manuel.frey@volvo.com.

‡Division Head, Space Propulsion, Lampoldshausen Research Center; wolfgang.koschel@dlr.de. Member AIAA.

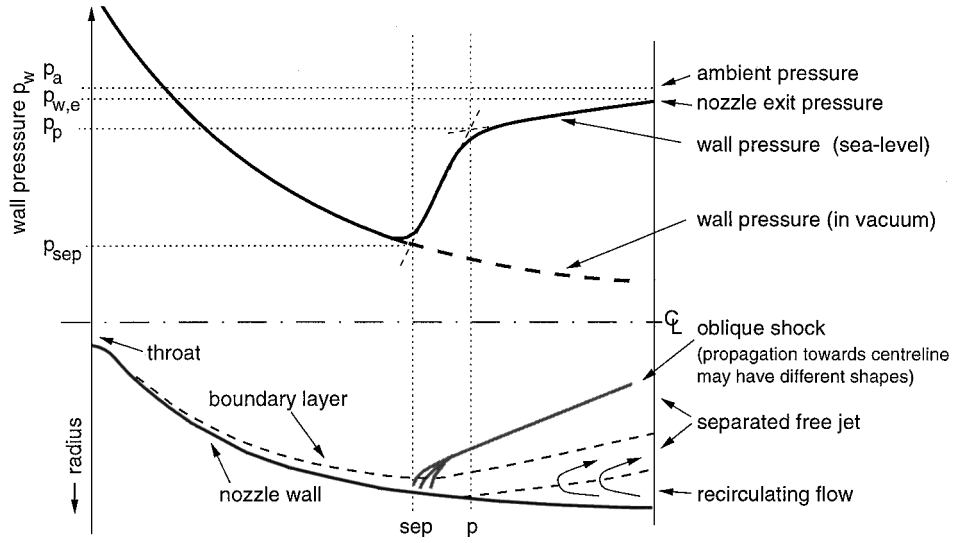

Fig. 1 Free shock separation, where the separated flow continues as a freejet—phenomenological sketch.

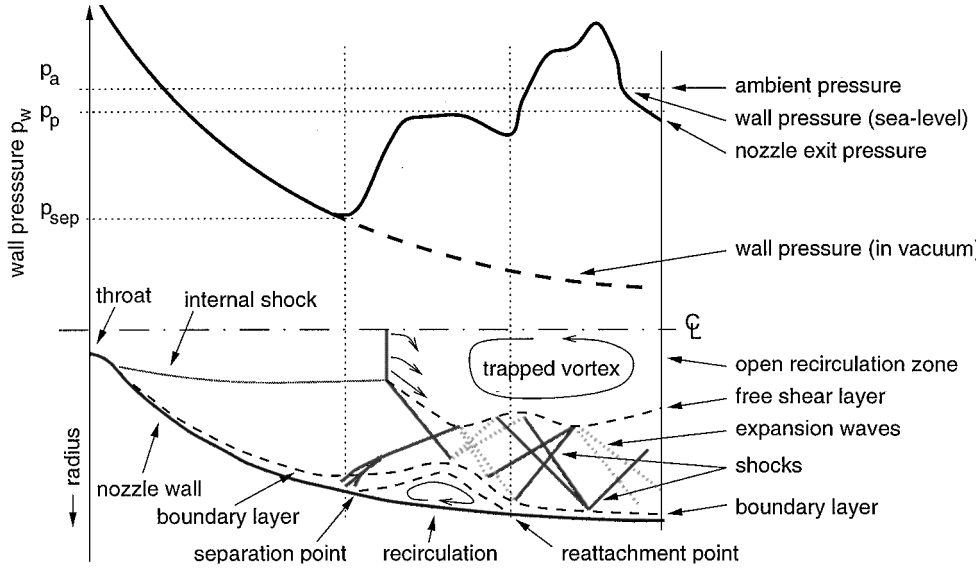

Fig. 2 Restricted shock separation (RSS), where the separated flow reattaches to the nozzle wall, thereby forming a closed recirculation bubble—phenomenological sketch.

pattern also occurs inside the nozzle.[5] In this case the cap-shock pattern induces a radial momentum toward the wall, which might promote a reattachment of the separated flow and hence results in the FSS → RSS transition. Figure 4 illustrates this momentum balance. Thus, it was concluded by the authors that transition from FSS to RSS and vice versa only depended on the type of nozzle contour, and not on the scale or the combustion gas properties.[5] This transition theory, meanwhile accepted in Europe,[4] has also been confirmed by subscale tests with a ceramic nozzle extension of Vulcain type contour,[10] with a geometric scale of 1:5. Plume flow with the cap-shock pattern was equal, and the FSS → RSS transition occurred during tests with staircase chamber pressure variation at the same pressure ratio as observed for the full-scale Vulcain nozzle.

In the following, the cap-shock pattern, the FSS → RSS transition, and the side-load behavior of thrust-optimized and parabolic nozzles are thoroughly discussed by means of analytical considerations and subscale cold-gas test results.

Cap-Shock Pattern

Different shock patterns can be observed in the plume of overexpanded nozzles, depending on the nozzle type (plane or axisymmetric) and contour (thrust-optimized, truncated ideal, etc.). A very interesting shock pattern occurs in the plume of axisymmetric thrust-optimized or parabolic nozzles [e.g., Vulcain or space shuttle main engine (SSME)] at low pressure ratios p_c/p_a: the cap-shock pattern. Being the only one of all observed patterns that can substantially affect the wall pressure and hence influence thrust and side-force behavior, it is worth taking a closer look at this specific plume.

As mentioned in Ref. 5, the cap-shock pattern is only observed in the plume of thrust-optimized or parabolic rocket nozzles with a highly two-dimensional flowfield structure in the nozzle. The strong expansion along the circular arc contour in the nozzle throat with high initial angles up to 38 deg and the subsequent recompressing contour result in a high-Mach-number flowfield along the centerline, limited by an internal shock. This internal shock does not exist in truncated ideal nozzles, where the cap-shock pattern has never been observed. In conical nozzles a weak internal shock exists, but it intersects the centerline shortly downstream of the throat, hence preventing the formation of a high-Mach-number flow near the axis.[5] This explains why the cap-shock pattern has never been observed in conical nozzles either. As a consequence, it can be supposed that the internal shock is responsible for the cap-shock structure.

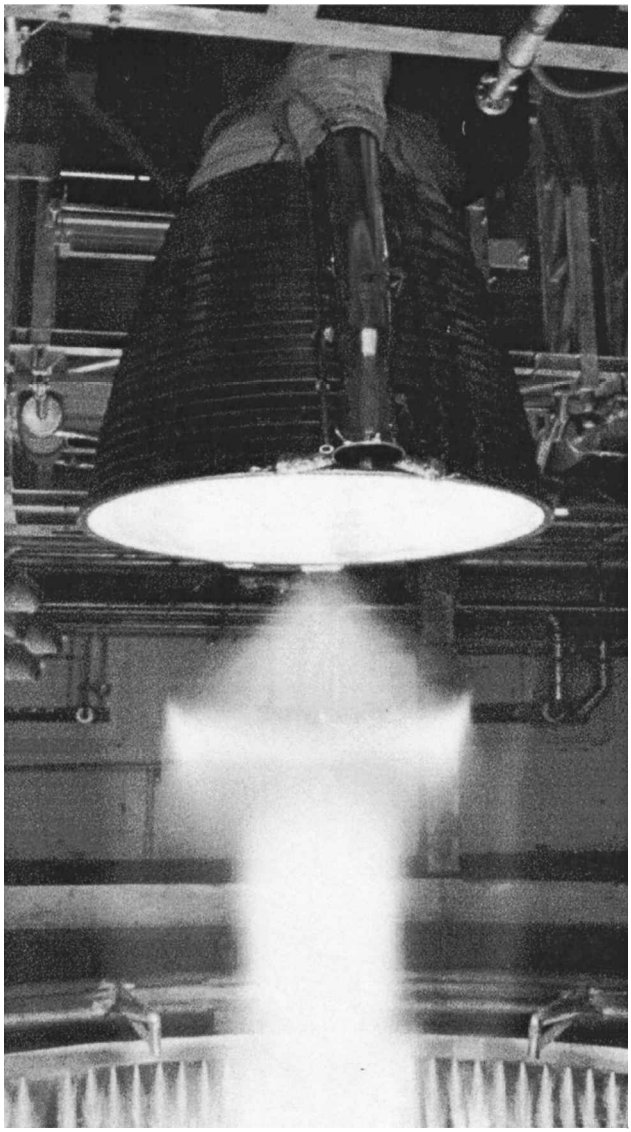

Fig. 3 Cap-shock pattern in the plume of the Vulcain engine during full-flowing operation.

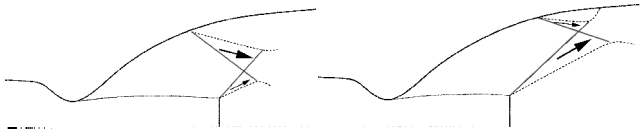

Fig. 4 Momentum balance across cap-shock system.

For a better understanding of the physics behind the cap-shock pattern, the flow in the Vulcain nozzle was numerically simulated using a finite volume scheme, which is described in detail in Ref. 11. Because a whole series of simulations was performed for different pressure ratios, the flow was assumed to be a perfect gas with a constant specific heat ratio $\gamma = 1.2$ in order to save computational time. Because of the unstructured, solution-adaptive grid, shocks and shear layers are well resolved, and a comparison between numerical simulation and photographs of the plume shows a good agreement.

The simulation for a pressure ratio $p_c/p_a = 100$ is used to investigate the character of the cap-shock pattern. Figure 5 shows the Mach-number distribution of the whole nozzle flow and additionally a zoom on the part of the cap-shocks near the centerline.

To check whether the cap-shock pattern can be interpreted as a reflection phenomenon of the internal shock at the centerline, a pressure deflection or heart diagram of the flow near the triple

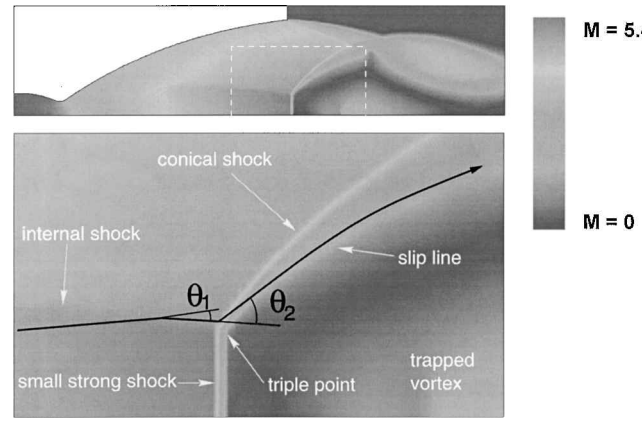

Fig. 5 Numerical simulation of the Vulcain nozzle flow for a pressure ratio p_c/p_a = 100—Mach-number distribution.

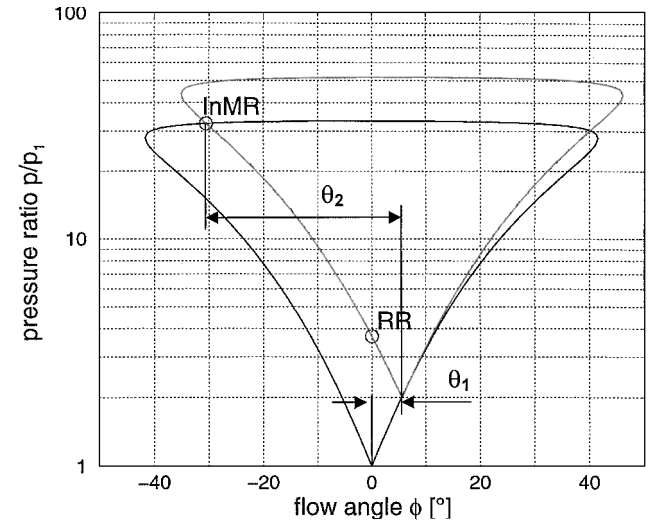

Fig. 6 Pressure deflection or heart diagram for the reflection of the internal shock at the centerline in the Vulcain nozzle—p_1 is the pressure upstream of the internal shock, and $\phi = 0$ deg is defined as the flow angle upstream of the internal shock.

point is established (see Fig. 6). However, strictly speaking, these diagrams are valid only for planar flows; if they are used to analyze axisymmetric problems as in our case, centerline effects can lead to solutions that slightly deviate from the predicted ones.

It is obvious from the numerical simulation shown in Fig. 5 that the shown case cannot be a regular reflection of the internal shock at the centerline because of the existence of a triple point, and so the point RR in Fig. 6 can be discarded as a solution. Nevertheless, a solution of this kind can be observed for higher pressure ratios after the cap-shock pattern has converted into a Mach disk. In this case the Mach disk is located downstream of the regular reflection point of the internal shock. It can also be seen from Fig. 6 that a usual Mach reflection of the internal shock at the centerline is not possible because the mechanical equilibrium condition (e.g., see Ref. 12) is not fulfilled, or in other words because the internal shock is too weak.

Still, the triple point indicates some kind of Mach reflection. However, there are some basic differences between the phenomenon shown in Fig. 5 and a usual Mach reflection of an incident shock at a symmetry plane or centerline:

1) The flow below the internal shock is divergent, and the strong shock below the triple point called "Mach stem" is straight. The grid in this region was refined several times, and no curvature of the stem occurred. This means that the stem is a straight shock at the centerline, but an oblique shock near the triple point. As a consequence,

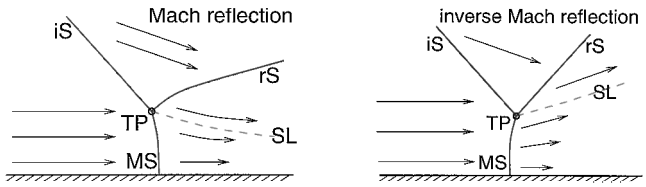

Fig. 7 Comparison between Mach reflection (left) and inverse Mach reflection (right) for parallel inflow—phenomenological sketches; iS, incident shock; rS, reflected shock; MS, Mach stem; SL, slip line; and TP, triple point.

the Mach stem is convex with respect to the streamlines if viewed from upstream (not with respect to the geometry). This is in contrast to usual Mach stems, which are always concave.

2) The Mach stem in Fig. 5 deflects the flow away from the axis, whereas usual Mach stems deflect the flow toward the axis. Therefore, the slip line downstream of the triple point also shows away from the axis.

3) Downstream of the Mach stem, a stable vortex is trapped in the case of the cap-shock pattern—a phenomenon that is unknown for usual Mach reflections.

For a better understanding both reflection phenomena are sketched also in Fig. 7 for an initially parallel flow.

The second item indicates that in the heart diagram a solution with negative flow angle $\phi = \theta_1 - \theta_2$ must be looked for. Indeed, a possible solution can be found at the inverse Mach reflection point, labelled InMR in Fig. 6. This is quite surprising because inverse Mach reflections are believed not to occur in stationary and pseudo-stationary flows.[12] Nevertheless, another case of stationary inverse Mach reflection has recently been reported in the literature: Gribben et al.'s[13] recalculation of Welsh's[14] experiment with an underexpanded nozzle flow also reveals a convex curvature of the Mach stem, hence a deflection away from the axis and even a trapped vortex. The results are confirmed by electron beam fluorescence pictures.

In the case of the Vulcain engine, a comparison between the results from the pressure-deflection diagram and the numerical simulation reveals a good agreement concerning Mach numbers and flow angles; the deviations, which are below 5%, are probably caused by centerline effects and the divergence of the flow upstream of the Mach stem. This confirms that the cap-shock pattern can be interpreted as an inverse Mach reflection of the internal shock at the centerline.

It is of special interest to consider what happens downstream of the inverse Mach reflection. The slip line, which originates from the triple point and is inclined away from the axis, is hit by the overexpansion shock and hence is deflected toward the axis. At the same time the pressure on the nozzle axis rises with increasing x position, forcing a flow near the axis against the main flow direction. Additionally, the strength of the small strong shock decreases from the axis (normal shock) to the triple point (strong oblique shock), hence inducing a vorticity according to Crocco's theorem.[15] As a result, a trapped vortex is established downstream of the small strong shock. Therefore, two stagnation points can be located on the axis: the first one closely downstream of the small strong shock, and the other one about one exit diameter behind the nozzle exit plane. A detailed description of this plume flow structure is given in Ref. 5. Because the trapped vortex was not only observed in the case of overexpanded thrust-optimized and parabolic nozzles, but also in the underexpanded jet flow described in Refs. 14 and 15, which also was identified to be an inverse Mach reflection, it can be anticipated that a trapped vortex is inherent to inverse Mach reflections.

Subscale Cold-Gas Test Campaign

It was supposed in Ref. 5 that truncated ideal nozzles produce much lower side loads than parabolic or thrust-optimized nozzles because of the reattachment of the supersonic flow to the wall for a certain pressure ratio range.

To explore the separation and side-load characteristics of both class of nozzle families, a cold-gas subscale test campaign has been initiated at DLR Lampoldshausens P6.2 test facility. The facility consists of a closed-altitude chamber with supersonic diffuser in which the test nozzle is mounted. The nozzle is fed with gaseous nitrogen at pressures up to $p_c = 60$ bar. As the nozzle exhaust flows through the diffuser, the pressure p_a in the altitude chamber decreases. Figure 8 illustrates the principle of this facility, and Ref. 16 gives a more detailed description. Pressure ratios of $p_c/p_a > 300$ can be achieved, depending on both nozzles and diffuser geometries.

The nozzle flowfield development is characterized by means of schlieren images, high-frequency wall-pressure measurements, and side-load measurements. Side loads are measured with strain gauges, which are mounted on a thin bending tube far upstream of the nozzle throat. Figure 9 shows the principle setup for the side-load measurement (see again Ref. 16 for further details on the measurement devices and calibrations).

For the tests at the P6.2, both a truncated ideal and a parabolic nozzle have been designed to enable a direct comparison of the side-load level in both contour types. The main design idea has been to compare two nozzles of identical surface area (and thus mass), identical vacuum performance $I_{sp,vac}$, and identical nozzle wall exit pressure $p_{w,exit}$, while the nozzle length l_{div} and the area ratio ε are not fixed.

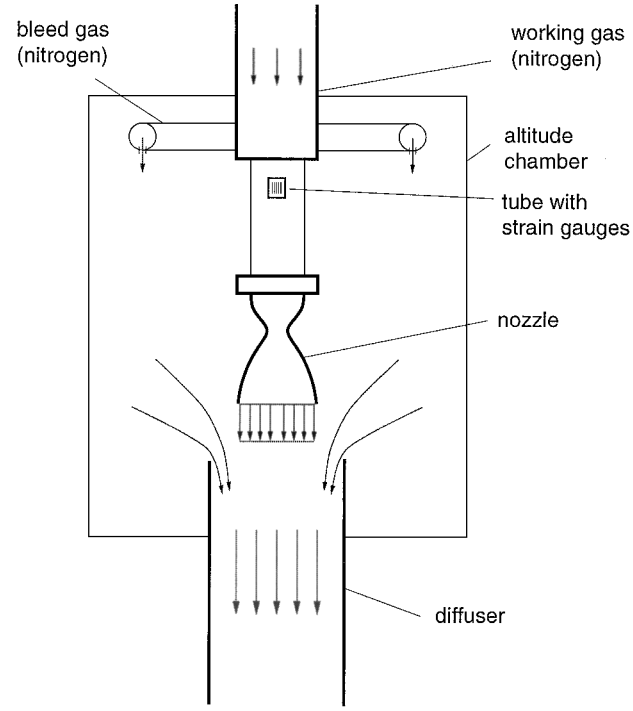

Fig. 8 Principle of the DLR P6.2 test facility.

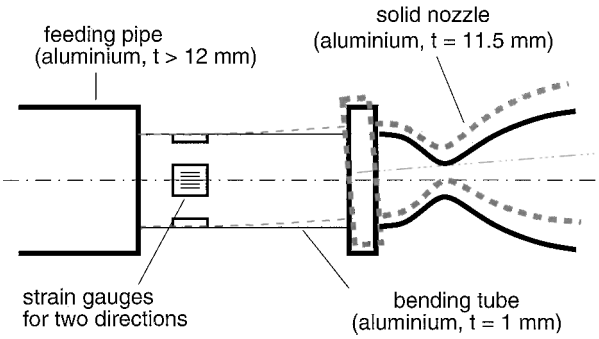

Fig. 9 Description of the bending tube used to measure the side-load torque.

Table 1 Geometrical design data of truncated ideal and thrust-optimized cold-gas subscale nozzle

Head	Truncated ideal nozzle	Parabolic nozzle
Throat radius, r_t	10 mm	10 mm
Area ratio, ε	20.66	30
Nozzle length, l/r_t	14.83	12.5

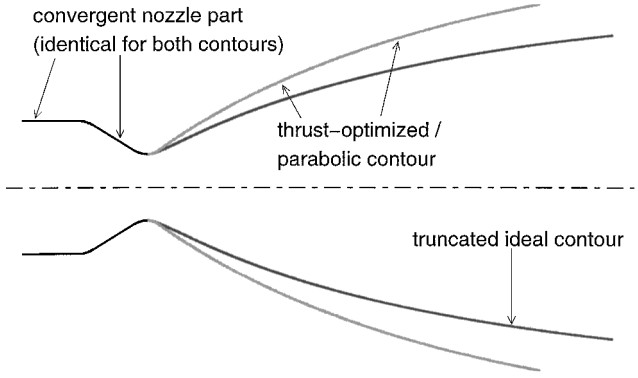

Fig. 10 Comparison of the two tested nozzles: truncated ideal contour and thrust-optimized contour.

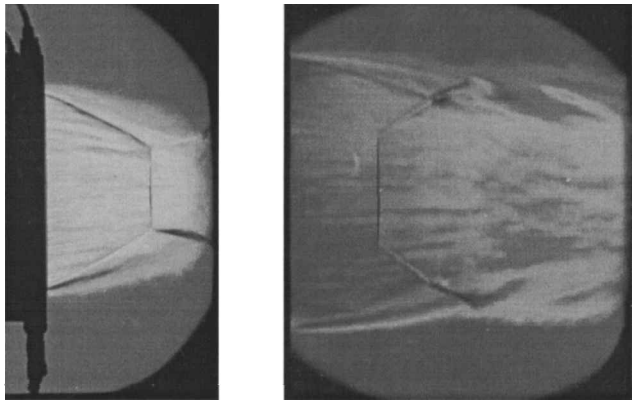

Fig. 11 Different plume pattern in P6.2 subscale nozzles: Mach disk in plume of truncated ideal nozzle (left) and cap-shock pattern in plume of thrust-optimized contour (right).

This means in terms of a launcher application both nozzles would feature an equal chamber pressure to achieve full flowing and an equal vacuum performance. A minor difference in sea-level performance must be taken into account, which however is of little importance in the case of central stage engine application of parallel-staged vehicles as it is, for example, for the SSME and the Vulcain engine, respectively.

Figure 10 compares both nozzle contours. Table 1 summarizes the main geometrical design data. This choice for the nozzle contour definition guarantees a very good comparability because the only substantial difference between both nozzles is the separation and side-load characteristic during startup and shutdown.

Figure 11 shows schlieren images of the exhaust flow plumes for both nozzles. In the case of the truncated ideal nozzle, the classical Mach disk is well visible, whereas the plume of the parabolic nozzle clearly features the aforementioned cap-shock pattern.

Figure 12 shows the measured wall pressures in the truncated ideal nozzle for a series of different chamber pressures. There is no difference in wall-pressure behavior between startup (increasing pressure ratio p_c/p_a) and shutdown (decreasing pressure ratio). (The ambient pressure used for normalization denotes the pressure in the altitude chamber, which is measured at different locations in the chamber. A comparison of tests with and without altitude chamber showed no difference in the p_w/p_a distribution for identical total pressure ratios p_c/p_a.) As expected, the measured wall-pressure behavior of the truncated ideal nozzle only shows the occurrence of FSS. Near the separation point the wall pressure suddenly increases from the vacuum profile to a plateau value. Downstream of this point, a recirculation region exists, in which the pressure is almost constant, increasing only slightly toward the nozzle exit. The pressure in this recirculation region clearly stays below the ambient pressure, reaching values of $0.95 \cdot p_a$.

In the parabolic nozzle RSS was observed for a certain pressure ratio range during startup and shutdown. In contrast to the truncated ideal nozzle, the wall-pressure distributions for startup and shutdown differ, as can be seen in Figs. 13 and 14. The difference is caused by a hysteresis in the pressure ratio at which transition occurs from FSS to RSS at startup and from RSS to FSS at shutdown.

In Fig. 13 the usual behavior for FSS can be initially observed (e.g., the wall-pressure behavior is comparable to the one of the truncated ideal nozzle, but only up to a pressure ratio of 32). When the pressure ratio increases above 32, a jump downstream of the separation point can be noticed. This phenomenon is induced by the reattachment of the flow to the wall, also indicated as RSS. A separation bubble forms, in which the pressure is lower than the ambient pressure. When the pressure ratio is further increased, the downstream end of the separation bubble will reach the nozzle exit, and the bubble will open, thereby inducing transition from RSS back to FSS. The pressure in the recirculation region then rises from the pressure in the separation bubble to a value close to the ambient pressure, causing the separation point to jump upstream. This can be seen in the curves for $p_c/p_a = 34$ and 40. For both pressure ratios the separation point lies at $x/r_t \sim 9.8$, indicating that the transition has happened between these pressure ratios.

At shutdown these phenomena will occur in reversed order, which can be seen in Fig. 14. The wall pressures for shutdown drawn here show the transition from FSS to RSS between the pressure ratios $p_c/p_a = 37$ and 34. At $p_c/p_a = 37$ there is still FSS with the separation point at $x/r_t \sim 8.9$, whereas at $p_c/p_a = 34$ the separation point has jumped downstream to $x/r_t \sim 9.8$. A separation bubble has then formed and persists down to a pressure ratio of 14. In the reattached flow a series of compressions and expansions causes an oscillatory behavior of the wall pressure, with peaks well above and below the ambient pressure (see Refs. 3–7 for further details).

At the pressure ratio of 14, the retransition to FSS occurs. Compared to the startup, it is clear that the separation with reattachment flow regime exists for a far larger range of pressure ratios at shutdown. The opening and closure of the separation bubble, respectively, occurs at the same pressure ratio for startup and shutdown, i.e., in between 34 and 37. The transition at lower pressure ratios, which is caused by the momentum toward the wall, shows a significant hysteresis—transition at $p_c/p_a \sim 32$ for startup and at $p_c/p_a \sim 14$ for shutdown. This hysteresis is explained in Ref. 5.

In the graphs for shutdown, the local wall pressure peaks downstream of the separation point reach values high above the ambient pressure, which are caused by the reattachment of the separated flow. Furthermore, the oscillatory behavior of the pressure caused by compression and expansion waves in the reattached flow is also clearly illustrated in the Fig. 14.

As explained before, the aerodynamic side-load torques have been recalculated from the strain gauge measurements. Figures 15 and 16 show the averaged aerodynamic torque for the truncated ideal nozzle and the thrust-optimized nozzle, over an averaging period of 0.25 s. At a low-pressure ratio of about 5, a side-load peak can be seen for the truncated ideal nozzle for both startup and shutdown. This peak occurs at all nozzles tested at the test facility P6.2 and has also been described in Refs. 17 and 18. The origin of this peak is subject of further investigation.

For the truncated ideal nozzle the aerodynamic torque gradually grows with increasing pressure ratio until a flat maximum is reached with the separation point at about one-third of the divergent nozzle length. Afterwards the side load decreases again with increasing pressure ratio. The side loads show identical behavior for startup and shutdown, as is the case for the measured wall pressure.

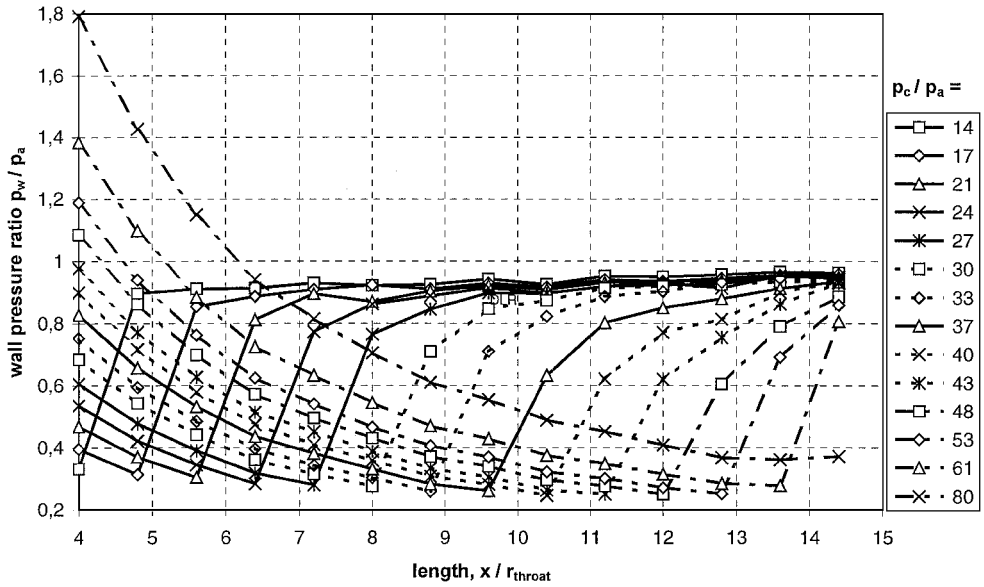

Fig. 12 Wall pressure in the truncated ideal nozzle.

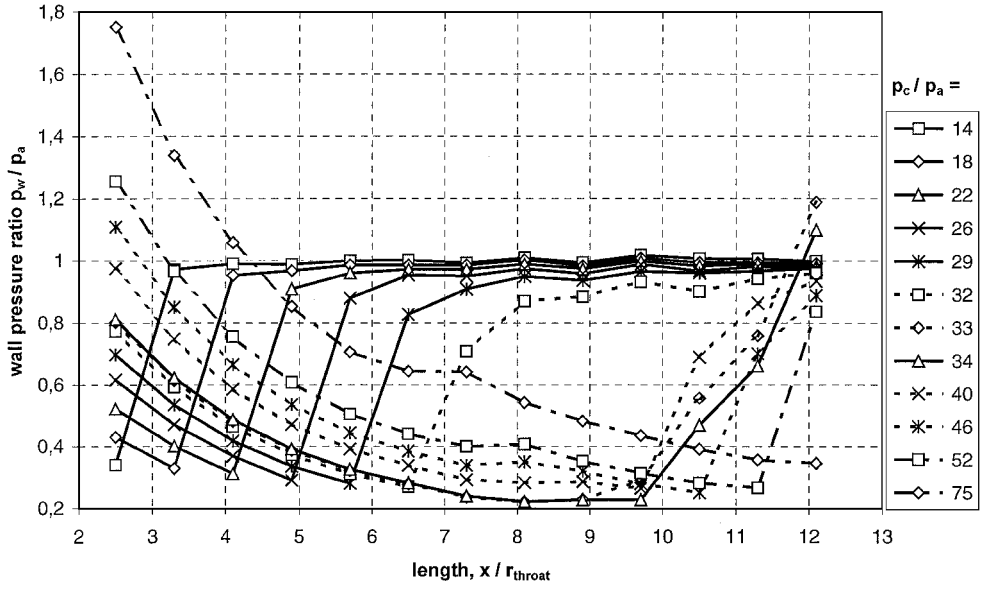

Fig. 13 Wall pressure in the thrust-optimized nozzle for startup.

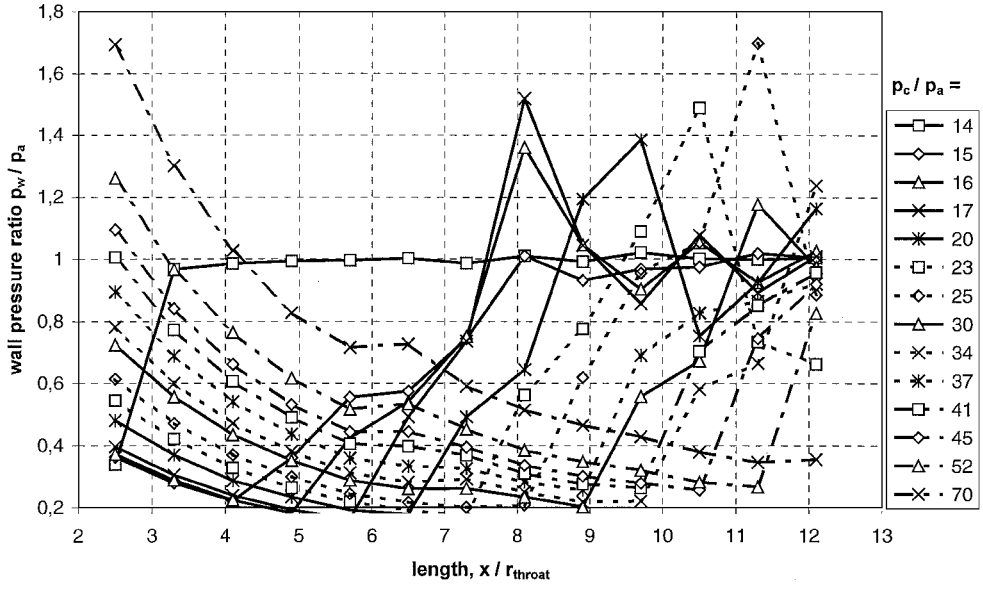

Fig. 14 Wall pressure in the thrust-optimized nozzle for shutdown.

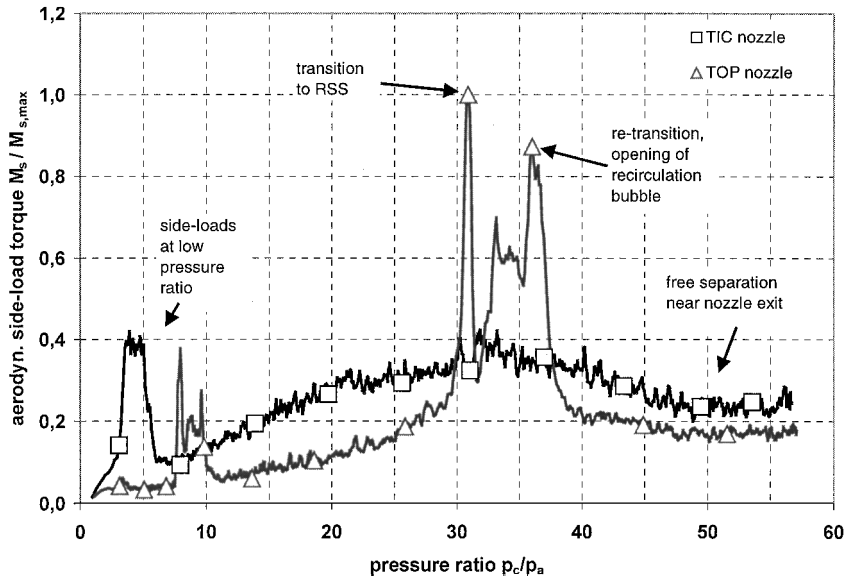

Fig. 15 Comparison between the averaged side-load torque of the truncated ideal and the thrust-optimized nozzle for increasing pressure ratio $\partial(p_c/p_a)/\partial t > 0$ (simulated startup).

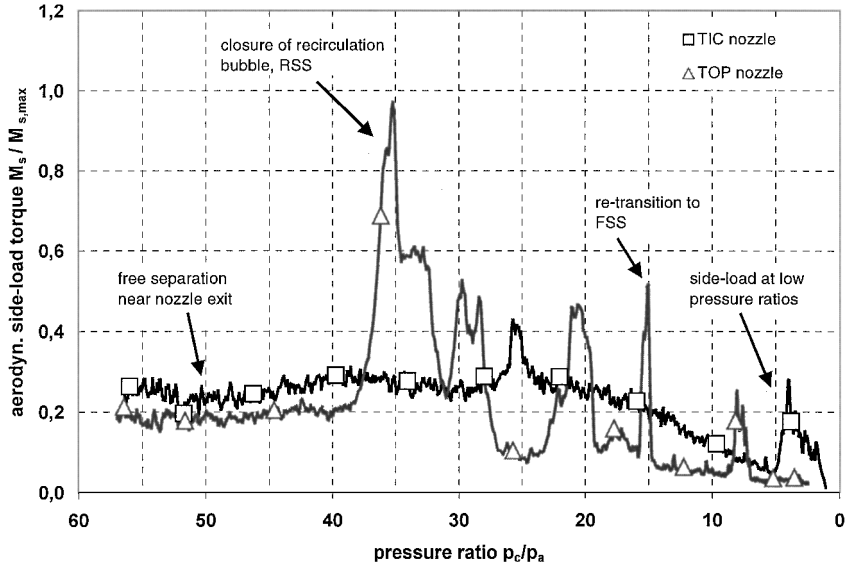

Fig. 16 Comparison between the averaged side-load torque of the truncated ideal and the thrust-optimized nozzle for decreasing pressure ratio $\partial(p_c/p_a)/\partial t < 0$ (simulated shutdown).

The side-load behavior of the thrust-optimized nozzles is very different from that of the truncated ideal nozzle. Going through the figure from left to right, i.e., first startup, then shutdown, the following can be noticed: in the FSS region the side load gradually increases with the pressure ratio until the flow changes to RSS. At the transition pressure ratio a huge side-load peak is induced. During the occurrence of RSS—only in a narrow range of pressure ratios during startup—some irregular side-load activity can be observed, which is clearly lower than the transition load. At a pressure ratio of about 37, another significant peak marks the opening of the separation bubble and the transition back to FSS. After this peak the side load gradually decreases with increasing pressure ratio.

Qualitatively the same behavior can be seen for shutdown. The hysteresis effect however causes the RSS region to be much larger than for startup. The closure of the separation bubble is marked by a huge side-load peak at $p_c/p_a \sim 37$. In the RSS region moderate side-load peaks are induced whenever a region of high wall pressure reaches the nozzle exit (e.g., $p_c/p_a \sim 29$ and 21). At $p_c/p_a \sim 15$ the retransition back to FSS occurs, which is again visible as a distinct activity in Fig. 15. The subsequent smooth FSS behavior is only disturbed by the low-pressure ratio peak.

Considering only the occurrence of FSS, the magnitude of the side-load torque is a bit lower for the thrust-optimized than for the truncated ideal nozzle. Taking into account the greater length of the latter, the applied forces might be about the same. However, the loads induced during the transition from FSS to RSS and the opening of the separation bubble reach values almost three times as high as the pure FSS loads of the truncated ideal nozzle.

Conclusions

The major origin for side loads in thrust-optimized and parabolic rocket nozzles is the transition between free shock separation, where the separated flow remains separated, and restricted shock separation, where the flow reattaches to the nozzle wall. This reattachment is caused by a special shock pattern, which can merely be observed in thrust-optimized and parabolic nozzles, the cap-shock pattern. It has been shown that this specific plume pattern can be interpreted as an inverse Mach reflection of the internal shock at the centerline.

Two different nozzle types, a truncated ideal and a thrust-optimized nozzle, have been tested at a cold-flow test facility to explore the different side-load origins. The experiments have proven

to be useful for the understanding and prediction of side loads in overexpanded nozzles.

In the FSS region the side loads for the truncated ideal nozzle are comparable to those of the thrust-optimized nozzle if the greater length of the former is taken into account. However, the overall comparison of lateral loads is dominated by the strong side-load peaks resulting from the transition between the different separation types in the thrust-optimized nozzle. These peaks reach a magnitude of about three times the side loads of the truncated ideal nozzle for equal pressure ratio.

Acknowledgments

This work has partly been financed by the German National Technology Program on Cryogenic Engine Research, TEKAN. A part of this work has been performed within the frame of the European Flow Separation Control Device Working Group. The authors acknowledge especially R. Ryden, T. Damgaard, and J. Östlund (Volvo Aero Corporation), Ph. James (SNECMA), Ph. Reijasse (ONERA), T. Alziary de Roquefort (University of Poitier), R. Schwane and J. Muylaert (European Space Research and Technology Centre), M. Pons, P. Vuillermoz, and N. Girard (Centre National d'Eludes Spatiales) and M. Terhardt (Astrium) for the fruitful cooperation in this field. Special thanks is addressed to R. Stark (DLR, German Aerospace Research Center) for his support in P6.2 testing of the truncated ideal contour and thrust-optimized contour nozzles.

References

[1]Nave, L. H., and Coffey, G. A., "Sea Level Side Loads in High-Area-Ratio Rocket Engines," AIAA Paper 73-1284, July 1973.

[2]Schmucker, R., "Stroemungsvorgaenge beim Betrieb Ueberexpandierter Duesen Chemischer Raketentriebwerke (Flow Processes in Overexpanded Nozzles of Chemical Rocket Engines)," Technical Univ. Munich, Rept. TB-7,-10,-14, Germany, July 1973 (in German).

[3]Frey, M., and Hagemann, G., "Flow Separation and Side-Loads in Rocket Nozzles," AIAA Paper 99-2815, June 1999.

[4]Hagemann, G., Terhardt, M., Frey, M., Oestlund, J., Onofri, M., Nasuti, F., and Reijasse, Ph., "Flow Separation and Side-Loads in Rocket Nozzles," *Proceedings of the 4th International Symposium on Liquid Space Propulsion*, DLR Lampoldshausen, March 2000.

[5]Frey, M., and Hagemann, G., "Restricted Shock Separation in Rocket Nozzles," *Journal of Propulsion and Power*, Vol. 16, No. 3, 2000, pp. 478–484.

[6]Mattsson, J., Högman, U., and Torngren, L., "A Sub-Scale Test Programme on Investigation of Flow Separation and Side-Loads in Rocket Nozzles," *Proceedings of the 3rd European Symposium on Aerothermodynamics of Space Vehicles*, ESA-ESTEC, ESA SP-426, Dec. 1998, pp. 373–378.

[7]Östlund, J., and Bigert, M., "A Subscale Investigation on Side-Loads in Sea Level Rocket Nozzles," AIAA Paper 99-2759, June 1999.

[8]Terhardt, M., Hagemann, G., and Frey, M., "Flow Separation and Side-Load Behaviour of the Vulcain Engine," AIAA Paper 99-2762, July 1999.

[9]Goel, P., and Jensen, R., "Numerical Analysis of the Performance of Altitude Compensating Dual-Bell Nozzle Flows," *32nd Jannaf Combustion Subcommittee Meeting and Propulsion Engineering Research Center—7th Annual Symposium*, CPIA Publ. 631, Vol. II, NASA MSFC, Oct. 1995, pp. 117–140.

[10]Alting, J., Grauer, F., Hagemann, G., and Kretschmer, J., "Subscale Tests with an Advanced 40 kN Thrust Chamber," AIAA Paper 2001-3260, July 2001.

[11]Hagemann, G., Schley, C.-A., Odintsov, E., and Sobatchkine, A., "Nozzle Flowfield Analysis with Particular Regard to 3D-Plug-Cluster Configurations," AIAA Paper 96-2954, July 1996.

[12]Ben-Dor, G., "Shock Wave Reflection Phenomena," Springer Publishing Company, New York, 1992.

[13]Gribben, B., Cantariti, F., Badcock, K., and Richards, B., "Numerical Study of an Underexpanded Jet," *Proceedings of the 3rd European Symposium on Aerothermodynamics of Space Vehicles*, ESA-ESTEC, ESA SP-426, Dec. 1998, pp. 111–118.

[14]Welsh, F., "Electron Beam Fluorescence Measurements of Shock Reflection Hysteresis in an Underexpanded Supersonic Jet," *Proceedings of the 21st International Symposium on Shock Waves*, Paper 5950, July 1997.

[15]Emanuel, G., *Gasdynamics: Theory and Applications*, AIAA Education Series, AIAA, New York, 1986.

[16]Frey, M., Stark, R., Ciezki, H. K., Quessard, F., and Kwan, W., "Subscale Nozzle Testing at the P6.2 Test Stand," AIAA Paper 2000-3886, July 2000.

[17]Arens, M., and Spiegler, E., "Shock-Induced Boundary Layer Separation in Overexpanded Conical Exhaust Nozzles," *AIAA Journal*, Vol. 1, No. 3, 1963, pp. 578–581.

[18]Lawrence, R., "Symmetrical and Unsymmetrical Flow Separation in Supersonic Nozzles," Ph.D. Thesis, Southern Methodist Univ., Dallas, April 1967.